Research Article

# Fabrication of ZnO Nanospikes and Nanopillars on ITO Glass by Templateless Seed-Layer-Free Electrodeposition and Their Field-Emission Properties

Debabrata Pradhan, Mukul Kumar, Yoshinori Ando, and K. T. Leung

*ACS Appl. Mater. Interfaces*, **2009**, 1 (4), 789-796• DOI: 10.1021/am800220v • Publication Date (Web): 18 March 2009



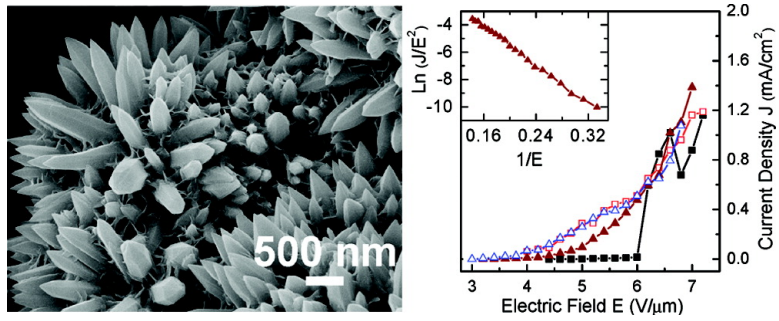


## More About This Article

Additional resources and features associated with this article are available within the HTML version:

- Supporting Information
- Access to high resolution figures
- Links to articles and content related to this article
- Copyright permission to reproduce figures and/or text from this article

View the Full Text HTML

# Fabrication of ZnO Nanospikes and Nanopillars on ITO Glass by Templateless Seed-Layer-Free Electrodeposition and Their Field-Emission Properties

**Debabrata Pradhan,[†] Mukul Kumar,[‡] Yoshinori Ando,[‡] and K. T. Leung*[,†]**

WATLab and Department of Chemistry, University of Waterloo, Waterloo, Ontario N2L 3G1, Canada, and Department of Materials Science and Engineering, Meijo University, Nagoya 468-8502, Japan

**ABSTRACT** A simple and direct electrodeposition technique is employed to fabricate ZnO nanospikes and nanopillars on indium−tin oxide glass substrates at 70 °C without using any template, catalyst, or seed layer. Both ZnO nanospikes and nanopillars exhibit highly crystalline ZnO wurtzite structure with a preferred (0001) plane orientation in their high-resolution transmission electron microscopic images and X-ray diffraction patterns. The corresponding Raman spectra provide evidence for the presence of defects and oxygen vacancies in these nanostructures, which could produce the photoluminescence observed in the visible region. X-ray photoelectron spectroscopy further indicates the presence of a $Zn(OH)_2$-rich surface region in these ZnO nanostructures and that a higher $Zn(OH)_2$ surface moiety is found for nanospikes than nanopillars. In contrast to the nanopillars with flat tops, the nanospikes with tapered tips of 20−50 nm diameter provide a favorable geometry to facilitate excellent field-emission performance, with a low turn-on electric field of 3.2 V/$\mu$m for 1.0 $\mu$A/cm$^2$ and a threshold field of 6.6 V/$\mu$m for 1.0 mA/cm$^2$. The superior field-emission property makes the nanospikes among the best ZnO field emitters fabricated on a glass substrate at low temperature.

**KEYWORDS:** zinc oxide • electrochemical deposition • nanostructured materials • field-emission properties • templateless • seed-layer-free growth

## 1. INTRODUCTION

Zinc oxide (ZnO), as a transparent semiconductor with a wide band gap of 3.4 eV and a large exciton binding energy of 60 meV at room temperature, is one of the most promising materials for a wide range of modern applications (1). With the development of film growth technologies and intense recent interest in nanotechnology, several varieties of ZnO nanostructured materials have been synthesized almost exclusively by thermal evaporation methods [particularly chemical vapor deposition (CVD)] (2), which generally require a high growth temperature above 550 °C. In contrast, wet chemistry techniques such as hydrothermal synthesis and electrodeposition are promising alternatives to synthesize ZnO nanostructures, especially at a significantly lower temperature (below 200 °C) (3, 4). Peulon and Lincot prepared ZnO nanowires on a tin-oxide-coated glass substrate for the first time using electrochemical deposition (at 80 °C) (5). Since then, several studies have been performed on these one-dimensional (1D) ZnO nanowires grown electrochemically (6) and hydrothermally (7, 8), which are mostly targeted for solar cell applications. Furthermore, 1D ZnO nanostructures are also known to be some of the best field emitters because of their high aspect ratios, making them a good choice for display applications. A striking advantage with ZnO lies in its high emission stability, in comparison to the well-studied carbon nanotubes, particularly in poor-vacuum and low-pressure air operating conditions (9). Given the large economic interest in fabricating field emission (FE) devices on low-cost glass substrates, the development of alternative methods to thermal evaporation would therefore be very useful. To date, there are only a limited number of reports on the FE properties of 1D ZnO nanostructures prepared by electrochemical deposition (10, 11) and hydrothermal synthesis (12−16), all of which exhibit a lower emission current density than those synthesized by thermal evaporation (17−26). In the present work, we synthesize two different types of 1D ZnO nanostructures, including nanospikes and nanopillars, by using direct electrodeposition, i.e., without the use of any template or catalyst or a ZnO seed layer. The nanospikes so prepared on indium−tin oxide (ITO)-coated glass substrates at 70 °C are found to exhibit better FE performance than other 1D ZnO nanostructures obtained by electrodeposition reported previously (10, 11). Furthermore, the FE performance obtained from the ZnO nanospikes in the present work also appears to be comparable to the best 1D ZnO emitters and is better than the majority of FE performances of these nanostructures synthesized on a silicon (or sapphire) substrate at a considerably higher temperature by thermal evaporation (17−29).

* Corresponding author. E-mail: tong@uwaterloo.ca.
Received for review December 6, 2008 and accepted February 18, 2009
[†] University of Waterloo.
[‡] Meijo University.
DOI: 10.1021/am800220v

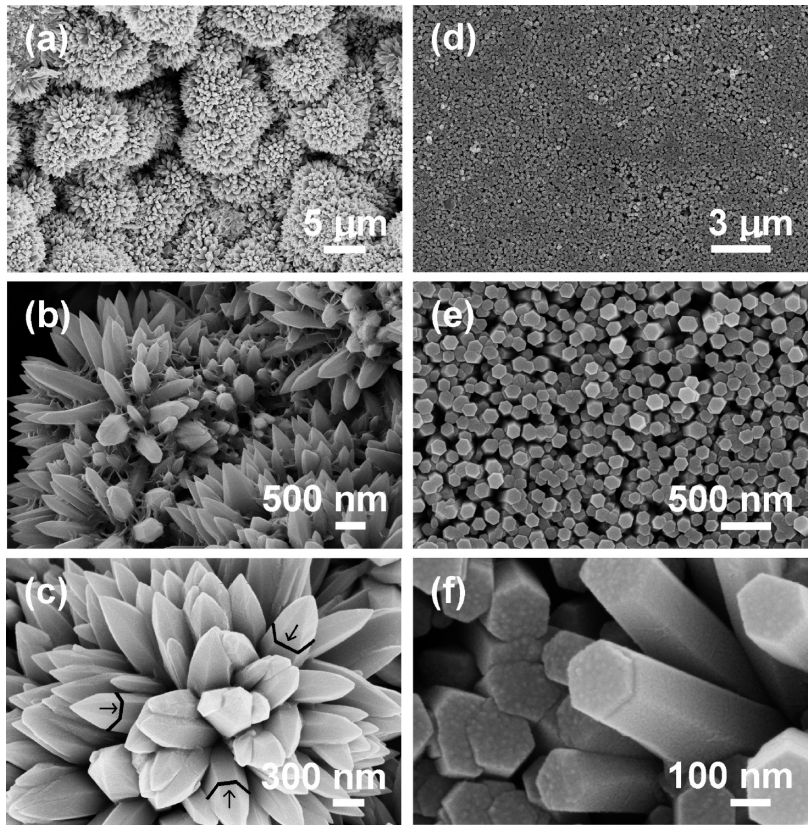


**FIGURE 1. SEM images collected at different magnifications of nanospikes (a−c) and nanopillars (d−f) electrodeposited on ITO glass at −1.1 V for 2 h at 70 °C in 0.01 and 0.001 M $Zn(NO_3)_2 \cdot 6H_2O$ mixed with 0.1 M KCl, respectively. The hexagonal shapes of the nanospikes are marked by arrows in part c.**

## 2. EXPERIMENTAL DETAILS

Details of the experimental setup and procedure have been given elsewhere (30). Briefly, the 1D ZnO nanostructures were deposited by amperometry potentiostatically at −1.1 V (with respect to a Ag/AgCl reference electrode) for 2 h on ITO glass substrates in a three-electrode cell immersed in a water bath held at 70 °C. The electrolyte consisted of a $Zn(NO_3)_2 \cdot 6H_2O$ solution at different concentrations (0.01 or 0.001 M) mixed with a 0.1 M KCl solution (acting as the supporting electrolyte). The morphology and crystallinity of the resulting ZnO nanostructures (electrodeposited on the ITO glass substrates) were characterized by using a LEO FESEM 1530 field emission scanning electron microscope (SEM) and a JEOL 2010 transmission electron microscope (TEM) operated at 200 kV and a PANalytical X'Pert Pro MRD X-ray diffractometer (XRD), respectively. The optical properties of the nanostructures were examined by using a Bruker Senterra Raman spectrometer with a 532-nm diode-laser excitation source operated at 20 mW, and a PerkinElmer LS 55 fluorescence spectrophotometer with a 250-nm excitation wavelength generated by a xenon lamp. The chemical-state surface composition of the ZnO nanostructures was analyzed by X-ray photoelectron spectroscopy (XPS) using a Thermo-VG Scientific ESCALab 250 Microprobe with a monochromatic Al Kα X-ray source (1486.6 eV). FE measurements of the as-grown 1D ZnO nanostructures were performed by using a conventional parallel-plate diode configuration, with the ZnO sample serving as the cathode and a stainless steel rod (with a flat circular base of 1.5-mm diameter) as the anode. The separation between the cathode and anode was kept constant at 0.5 mm, as measured by an optical microscope. The FE current was measured by using a Keithley 6485 picoammeter as a function of the negative voltage applied to the ZnO electrode at a typical chamber pressure of $2.2 \times 10^{-6}$ Torr.

## 3. RESULTS AND DISCUSSION

**3.1. Morphology, Crystal Structure, and Chemical-State Composition.** Figure 1 shows the SEM images, collected at different magnifications, of the ZnO nanospikes and nanopillars electrodeposited on ITO glass for 2 h at 70 °C using respectively a 0.01 and 0.001 M $Zn(NO_3)_2 \cdot 6H_2O$ solutions mixed with 0.1 M KCl. The nanospikes are found to largely grow in globular bunches with diameters of 5−8 $\mu$m (Figure 1a). The nanospikes in each globular bunch appear to be connected together by very fine threads of diameter of less than 10 nm (Figure 1b). Individual nanospikes (in the globular bunches) are found to have hexagonal trunks of 200−400 nm average diameter tapering to sharp tips of 20−50 nm diameter (Figure 1c). Although there have been previous studies on the formation of ZnO nanostructures with similar shapes, including nanopins (23) and nanoneedles (26), obtained by thermal evaporation techniques, the closest 1D ZnO nanostructure (with similar shape) obtained by an electrochemical technique was the cathodic deposition of ZnO nanoneedles reported by Cao et al., which required the use of a gold layer deposited (on their silicon substrate) prior to growth (31). In the present work, we therefore demonstrate that the successful formation of nanospikes can be achieved for the first time by electrodeposition without any gold layer by judicious choice of optimum electrolyte concentration and applied potential.

The deposition of nanopillars is found to be reasonably uniform over a large area (>1 $cm^2$; Figure 1d−f), with

individual pillars appearing with a well-defined hexagonal shape (Figure 1f). The typical dimensions of individual nanopillars are 100−120 nm in diameter and 600 nm in length (the length is estimated from the vertically tilted or fallen pillars located at the edge of the substrate shown in Figure 1f). In a recent study, Chen et al. obtained nanopillars of larger diameters (100−250 nm) at a lower density on ITO glass using the same electrolyte at the same concentration, with the majority of the nanopillars not being vertically aligned (32). However, higher degrees of orientation and alignment of ZnO nanorods have been observed on a GaN single crystal by Pauporte et al. (33) and on ZnO-seeded layers by Cao et al. (10), which suggests that close matching in the lattice parameters may be responsible for the better morphology alignment. The present work therefore demonstrates that highly oriented and well-aligned ZnO nanopillars can be grown on virgin ITO glass by using an appropriate electrode potential and an optimum electrolyte concentration. The length and, to a certain extent, the density of these nanopillars can also be controlled by varying the deposition time.

The formation of globular bunches of nanospikes indicates nonuniform nucleation on the substrate surface and faster growth kinetics from individual nucleation centers, which is due to a higher electrolyte concentration [0.01 M $Zn(NO_3)_2 \cdot 6H_2O$] used for the nanospikes growth. The hexagonal trunks of individual nanospikes indicate the inherent hexagonal crystal structure of ZnO. However, the possible reason for the termination of nanospikes growth with sharp tips is not known. Unlike the case of nanospikes, a lower electrolyte concentration [0.001 M $Zn(NO_3)_2 \cdot 6H_2O$] used for the growth of nanopillars produces more uniform nucleation and growth. The lower electrolyte concentration used for the electrodeposition leads to slower growth kinetics, which facilitates layer-by-layer growth of hexagonal plates in the nanopillars. This could be one of the reasons for the formation of flat tops of hexagonal nanopillars, in contrast to the case of nanospikes.

Figure 2 shows the high-resolution TEM (HRTEM) images taken from the edges of the nanospikes and nanopillars. The two-dimensional lattice patterns, with an interlayer spacing of 2.6 Å measured from the respective HRTEM images, show the highly crystalline nature of both the nanospikes and nanopillars, with growth occurring along the [0001] direction. The corresponding selected-area electron diffraction patterns (not shown) reveal spot patterns, further confirming the single crystalline nature of the nanospikes and nanopillars.

Figure 3 shows the corresponding XRD patterns of ZnO nanospikes and nanopillars obtained in glancing-incidence mode (with $\omega = 0.3°$). The positions of the major peaks assigned in the figure are well matched to those of the reference wurtzite structure of a ZnO powder (JDPDS 01-076-0704) (34), as shown in Figure 3c. The unassigned smaller XRD features belong to underlying ITO glass substrates. For nanopillars (Figure 3b), the strongest peak observed at 34.45° is attributed to (002), in good accord with the well-known observation that 1D ZnO nanostructures

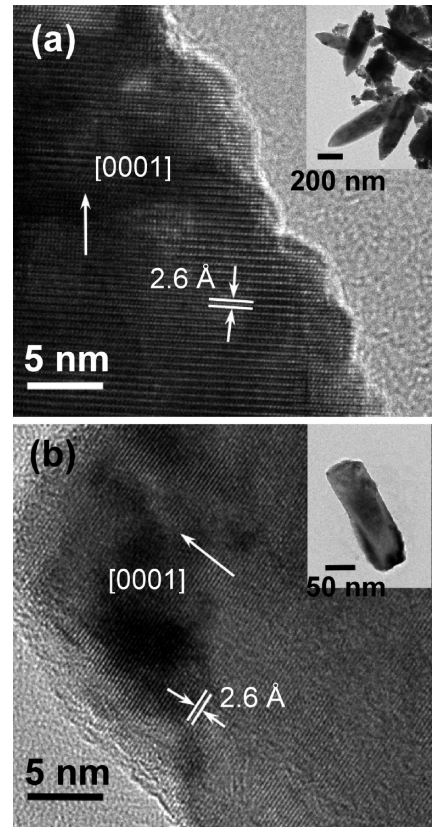


**FIGURE 2. HRTEM images of (a) nanospikes and (b) nanopillars, revealing the lattice spacing. The insets show the corresponding low-magnification TEM images.**

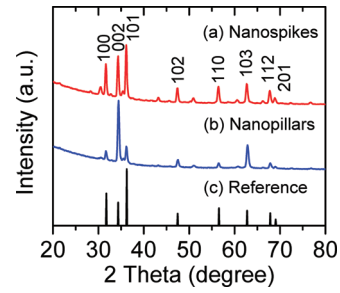


**FIGURE 3. Glancing-incidence XRD spectra of (a) ZnO nanospikes and (b) nanopillars electrodeposited on ITO glass at 70 °C. The crystallographic identifications of the ZnO peaks are labeled in accordance with (c) the reference spectrum for a ZnO powder (JCPDS 01-076-0704).**

(including nanorods and nanowires) prefer to grow along the *c* axis, i.e., in the (002) orientation (normal to the substrate) (35). In the case of nanospikes, other features from the (101) and (100) planes, in addition to the (002) plane, become similarly prominent (Figure 3a), which is due to the radial orientations of nanospikes (in the globular bunches). A similar observation of these additional features has been made in the case of randomly oriented ZnO nanowires (36). In contrast, the (002) plane becomes the singularly most intense feature for nanopillars, indicating its better orientation and alignments along the *c* axis. The other less intense ZnO diffraction features correspond to the presence of a small fraction of the nonvertical nanopillars.

Figure 4 compares the O 1s XPS spectra of nanospikes and nanopillars after brief (60 s) argon sputtering to remove

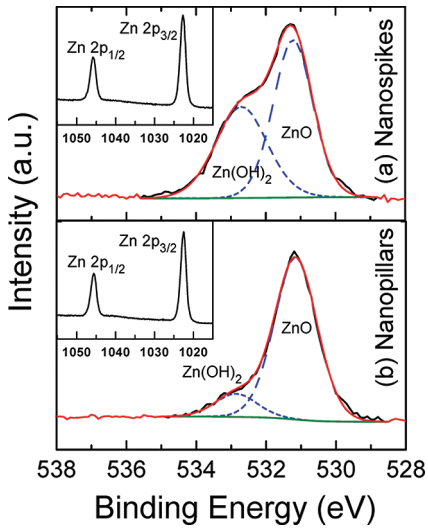


**FIGURE 4. O 1s XPS spectra of (a) nanospikes and (b) nanopillars (after 60 s of sputtering) deposited on ITO glass at 70 °C. The insets show the corresponding Zn 2p spectra.**

the surface contamination and the $Zn(OH)_2$-rich surface region. Using the Casa-XPS program, we fit the O 1s envelope with two components corresponding to $Zn(OH)_2$ at a higher binding energy (532.7 ± 0.1 eV) and ZnO at a lower binding energy (531.2 ± 0.1 eV). The binding energy difference between the two observed O 1s components is found to be within the range of literature values (1.5−2.0 eV) for reference ZnO samples (37, 38). It should be noted that these two components are also commonly found in the XPS spectra of ZnO films and powders (39, 40). In addition, the O 1s spectra evidently show a higher $Zn(OH)_2$ mole percent in nanospikes than nanopillars. This could be attributed to a higher electrolyte concentration (0.01 M) used to synthesize nanospikes than nanopillars (0.001 M), which resulted in the formation of a larger amount of $Zn(OH)_2$ before complete conversion of $Zn(OH)_2$ to ZnO. The insets of Figure 4 show the intense Zn $2p_{3/2}$ ($2p_{1/2}$) feature at 1022.5 eV (1045.6 eV), indicating the presence of a single $Zn^{2+}$ divalent state corresponding to both $Zn(OH)_2$ and ZnO. The observed spin−orbit splitting of 23.0 ± 0.1 eV is found to be in good accord with the literature value of 22.97 eV (41).

**3.2. Optical Properties.** Raman scattering is generally sensitive to the structural properties including atomic vacancy and defects and also to the sizes and shapes of the nanoscale materials. The structure of any material predominantly depends on the nature of the preparation methods and their corresponding parameters. Although there are several reports on the Raman scattering from ZnO single-crystal (42, 43) and ZnO nanomaterials synthesized by thermal evaporation methods (44, 45), relatively few studies have been conducted on ZnO nanostructures obtained by electrodeposition (46, 47). Figure 5 shows the Raman spectra of the nanospikes (Figure 1a−c) and nanopillars (Figure 1d−f) as electrodeposited on ITO glass. The Raman spectrum of a bare ITO glass substrate (Figure 5c) is also displayed for comparison. As ZnO belongs to the space group $P6_3mc$ or $C_{6v}^4$, there should be four Raman-active modes, $A_1 + E_1 + 2E_2$, that can be measured in the backscattering geometry with unpolarized light (42).

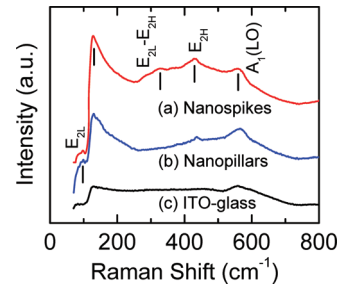


**FIGURE 5. Raman spectra of (a) nanospikes and (b) nanopillars electrodeposited on (c) an ITO glass substrate at 70 °C.**

**Table 1. Comparison of Peak Locations (in $cm^{-1}$) of Raman-Active Phonon Modes from ZnO Nanospikes and Nanopillars, Measured at Ambient Conditions, with Literature Values**

| | peak location ($cm^{-1}$) | | |
|---|---|---|---|
| mode | nanospikes | nanopillars | literature |
| $E_{2L}$ | 98 | 99 | 99 (51), 101 (42, 52), 102 (53) |
| plasma | 131 | 130 | 131 (46) |
| $E_{2L}-E_{2H}$ | 328 | | 331 (48), 334 (54) |
| $E_{2H}$ | 431 | 437 | 436 (48), 437 (42, 52), 439 (53) |
| $A_1$(LO) | 558 | 566 | 574 (42, 52, 53) |

The different Raman bands observed in the present study are assigned based on the zone-center optical phonons in ZnO reported in the literature (42, 51−53), which are summarized in Table 1. The origin of the strong band near 130 $cm^{-1}$ (Figure 4a,b) is not well understood, but it has been previously observed from ZnO nanoparticles and thought to be related to a plasma line from laser excitation (46). It should be noted that this strong band at 130 $cm^{-1}$ appears on top of the background with a rising edge also near 130 $cm^{-1}$ as exhibited by the ITO glass (Figure 5c). The other discernible Raman peaks common to both nanospikes and nanopillars correspond to the weak $E_{2L}$ or $E_2$(low) (respectively at 98.0 and 99.2 $cm^{-1}$) and $E_{2H}$ or $E_2$(high) features (at 430.5 and 437.4 $cm^{-1}$) and the broad $A_1$(LO) band (at 557.5 and 565.8 $cm^{-1}$). The weak broad ($E_{2L}-E_{2H}$) feature at 328 $cm^{-1}$ is only observed in the case of nanospikes (and not in nanopillars likely because of their weaker $E_{2L}$ and $E_{2H}$ modes), while a similar feature found for the ZnO crystal has been previously attributed to a multiphonon process by Damen et al. (42). Observation of broader $E_{2H}$ modes from both nanospikes and nanopillars in comparison to 1D nanostructures obtained by thermal evaporation methods (45) indicates the presence of inherently more defects and vacancies inside these nanomaterials electrochemically synthesized at a lower temperature. Although our XRD data show sharp diffraction features, the broad features in the Raman spectra indicate the presence of defects and vacancies due to the higher sensitivity of Raman scattering to crystal imperfections. For electrochemically synthesized "nanocolumnar" ZnO thin films, Mari et al. have reported an increase in the intensity of the $E_{2H}$ phonon mode upon postannealing and attributed it to an increase in crystallinity (47). The shifts of the $E_{2H}$ phonon mode toward lower wavenumbers generally indicate increasing amounts of strains and defects in these materials (48, 49). In the present

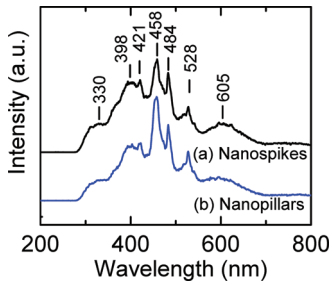


**FIGURE 6. PL spectra of ZnO (a) nanospikes and (b) nanopillars electrodeposited on ITO glass at 70 °C.**

work, the substantial shift of the $E_{2H}$ mode toward the lower wavenumber observed for nanospikes than nanopillars suggests a correspondingly higher defect density. Similarly, observation of the broad Raman phonon modes for nanospikes and nanopillars at a lower wavenumber (~560 $cm^{-1}$) than the most reported values (574 $cm^{-1}$) can also indicate oxygen vacancies (43) or disorder-activated Raman scattering (50).

The corresponding photoluminescence (PL) spectra of nanospikes and nanopillars obtained by the aforementioned electrodeposition, after appropriate removal of the very weak PL spectrum of bare ITO glass, are shown in Figure 6. Evidently, in addition to the commonly found broad PL background rising at 300 nm (55), both 1D ZnO nanostructures are found to exhibit similar PL features, including strong peaks at 458 and 484 nm and considerably weaker and broader features at 398, 421, and 528 nm. Although a large number of studies have been performed on the PL properties of ZnO in recent years, there are still contradictory explanations for the observed PL features (56). The PL emissions in different regions can be generally attributed to the shape and size of the nanostructures, as well as the oxygen contents and defects inside the material. In particular, ZnO nanostructures normally exhibit a strong UV luminescence line at ~380 nm (57, 58) and several luminescence features in the visible region, depending on the types of intrinsic defects or vacancies present in the material (59). The UV emission at ~380 nm is related to exciton recombination near the band edge of ZnO (60) and is found to be red-shifted to 398 nm for nanospikes and nanopillars obtained in the present work. In addition to the green PL feature, luminescence in the violet and blue regions is also known to occur (56). The violet PL peak at 421 nm from nanospikes or nanopillars in the present study is relatively weak compared to the respective blue PL feature at 458 nm, and it has been attributed to the presence of defects related to the zinc and oxygen vacancies (61, 62). Similarly, the blue PL feature at 458 nm could be due to zinc vacancies (55). The emission at 484 nm could also be assigned to an oxygen vacancy (61) and defects (62). Furthermore, the distinct, most commonly found green PL feature at 528 nm is due to the electron transition from a singly ionized oxygen vacancy to a photoexcited hole (63). The relatively broad PL band observed at 605 nm (yellow-orange emission) has also been previously reported, and their origin remains unclear (59). The observed visible PL features in the present work are therefore consistent with the generally broad features found in our Raman spectra (Figure 5), which both confirm the ready formation of defects expected at the lower temperature in the electrochemical synthesis for these nanomaterials.

**3.3. FE Properties.** Figure 7 shows the FE current density $J$ as a function of the applied field $E$ for nanospikes and nanopillars (Figure 1). The applied field is increased in the first ramp up (first up) and then decreased in the first ramp down (first down) and is repeated in the second cycle. The current density observed for nanospikes (Figure 7a) is evidently 2 orders of magnitude higher than that for nanopillars (Figure 7b). An abrupt increase in the current density with notable fluctuations is observed in the first-up applied field for nanospikes and nanopillars. A more stable change in the current density is measured in the subsequent steps. The first-up applied field is believed to remove the surface contaminants or amorphous hydroxide layer, thereby allowing the crystalline ZnO to emit electrons reproducibly during the rest of the cycles. The turn-on field (taken to be the field at a current density of 1 $\mu A/cm^2$) is measured to be 3.2 and 6.2 V/$\mu$m (from the second-up step) for nanospikes and nanopillars, respectively. The insets of Figure 7 show the corresponding Fowler–Nordheim (F–N) plots for nanospikes and nanopillars. According to the F–N relationship

$$J = \frac{A\beta^2 E^2}{\phi} \exp\left(-\frac{B\phi^{3/2}}{\beta E}\right)$$

where $J$ is the current density in units of $A/m^2$, $E$ is the applied electric field in units of V/m, $\phi$ is the work function of the emitter material in units of eV (5.3 eV for ZnO), and the constants $A = 1.54 \times 10^{-6}$ A eV $V^{-2}$ and $B = 6.83 \times 10^9$ $eV^{-3/2}$ V $m^{-1}$, we can obtain the field enhancement factor $\beta$ by

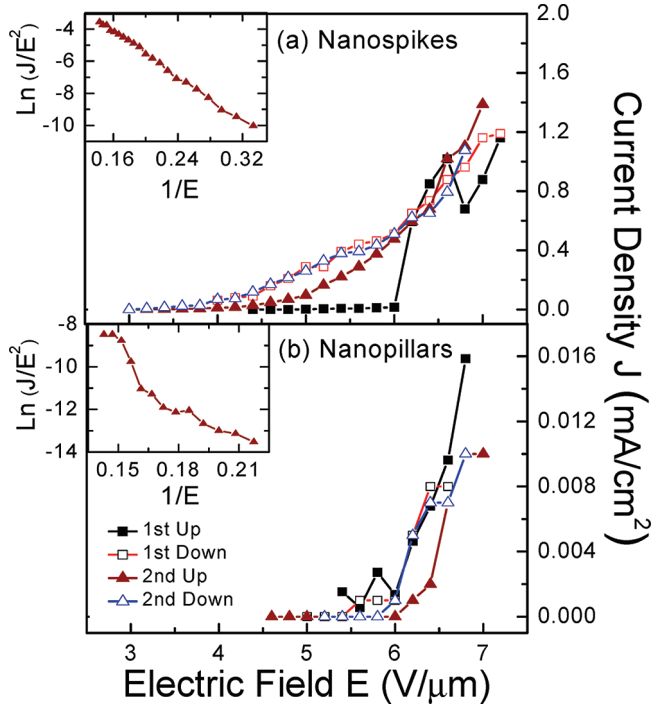


**FIGURE 7. FE $J$–$E$ characteristics of (a) ZnO nanospikes and (b) nanopillars, electrodeposited on ITO glass at 70 °C. The insets show the respective F–N plots of $\ln(J/E^2)$ versus $1/E$ for the second-up applied field.**

**Table 2. Performance Parameters of ZnO Nanostructured Electron Field Emitters[a]**

| ZnO nanostructure | turn-on field (V/$\mu$m) | threshold field (V/$\mu$m) | $\beta$ | $T$ (°C) | substrate [method][b] |
|---|---|---|---|---|---|
| nanospikes (this work) | 3.2 (1 $\mu$A/cm$^2$) | 6.6 | 2364 | 70 | ITO glass [ECD] |
| nanowires | 15.5/9.5 (10 $\mu$A/cm$^2$) | 18 (<250 $\mu$A/cm$^2$) | 1334 | 70 | ITO glass [ECD] (10) |
| nanowire arrays | 3.9 (1 $\mu$A/cm$^2$) | 4.8 (14 $\mu$A/cm$^2$) | 1339 | 65 | Cu/Si [ECD] (11) |
| nanoneedles | 4.2 (10 $\mu$A/cm$^2$) | 7.2 | 2350 | 70 | FeCoNi alloy [HS] (12) |
| prismatic nanorods | 6.4 (10 $\mu$A/cm$^2$) | 8.2 | 792 | | |
| nanotubes | 7.0 | 17.8 | 910 | 95 | Cu [HS] (13) |
| nanonunchakus | 3.0 | 5.47 | 1590 | 95 | p-Si [HS] (14) |
| nanorods with Pt/Ag nanoparticles | 2.0 | 2.0 | 7000 | 90−98 | Si/ZnO [HS] (15) |
| nanoneedles | 2.3 | 4.2 (<75 $\mu$A/cm$^2$) | 2080 | 100−160 | Si [HS] (16) |
| nanorods | 2.5 | 5.0 (<75 $\mu$A/cm$^2$) | 2040 | | |
| nanowire arrays | 7.1 (10 $\mu$A/cm$^2$) | 13.0 (10 mA/cm$^2$) | 862 | 80 | Si [HS] (64) |
| nanorods | 6.5 (10 $\mu$A/cm$^2$) | 9.8 (10 mA/cm$^2$) | | 250 | p-Si/AAO [ALD] (65) |
| nanoneedles | 4.1 | 9.6 | 1134 | 200 | polyamide [FCVA] (66) |
| nanorod arrays | 2.3 (1 $\mu$A/cm$^2$) | 4.2 | 2014 | 850 | Si/ZnO [CVD] (17) |
| injector-like nanowires | 1.85 (10 $\mu$A/cm$^2$) | 4.7 | 4386 | 580 | n-Si(111) [CVD] (18) |
| nanobelt | 2.3 | 5.3 | 6720 | 700 | brass [CVD] (19) |
| agavelike nanowires | 2.4 | 4.3 | 6041 | 975 | a-C/Si [CVD] (20) |
| nanowires | 0.2 | 0.7 | 41 000 | 725 | C-cloth [CVD] (21, 67) |
| nanobelts | 1.3 (10 $\mu$A/cm$^2$) | 2.9 | 14 000 | 800 | Au [CVD] (22) |
| nanopins | 1.92 | 5.9 | 657 | 600 | Si/Cu [CVD] (23) |
| tetrapod nanoneedles | 1.8 (1 $\mu$A/cm$^2$) | 3.9 | | 900 | quartz [CVD] (24) |
| microtowers | 1.8 | 4.8 | 3105 | 550 | Si [CVD] (25) |
| nanonails | 3.8 | 9.6 | 1450 | | |
| nanoneedles | 0.85 | 5.0 | 8328 | 500 | n-Si/Ti/Au [CVD] (26) |
| nanopencils | 3.7 (10 $\mu$A/cm$^2$) | 4.6 (1.3 mA/cm$^2$) | 2300 | 550 | n-Si [CVD] (68) |
| nanoscrews | 3.6 (10 $\mu$A/cm$^2$) | 11.2 (1.2 mA/cm$^2$) | | 480 | Si(100) [CVD] (69) |

[a] The turn-on and threshold fields are measured at current densities of 0.1 and 1.0 mA/cm$^2$, respectively, unless otherwise given in parentheses. The deposition temperatures ($T$) and the substrates used for the synthesis methods (identified in square brackets) are also given. [b] ECD: electrochemical deposition. HS: hydrothermal synthesis. ALD: atomic layer deposition. FCVA: filtered cathodic vacuum arc deposition. CVD: chemical vapor deposition.

plotting ln($J/E^2$) against 1/$E$. The $\beta$ factors for nanospikes and nanopillars are calculated to be 2364 and 1170, respectively, from the slopes of the straight lines of the respective F−N plots. The calculated $\beta$ values are therefore generally in the same range as that reported for ZnO nanowires (300−2000) (10, 13, 14, 16, 17). For a nanostructured emitter, the $\beta$ factor is related to the geometry (aspect ratio), work function, conductivity, and density of the nanostructures. The higher the field enhancement factor, the better is the emission.

Table 2 compares the characteristic FE properties measured by using the parallel-plate configuration for different ZnO nanostructured field emitters. We have included all of the ZnO nanostructures synthesized at low temperature by the wet chemistry methods (10−16, 64). Out of the over 50 studies on ZnO field emitters synthesized at high temperature by the thermal evaporation methods in the past 5 years, we include only the 20% of these studies that report the best FE performance with a turn-on field lower than 5.0 V/$\mu$m (at 0.1 $\mu$A/cm$^2$) (17−26). Evidently, the FE performance of ZnO nanostructures obtained by wet chemistry methods is generally poorer than those obtained by thermal evaporation techniques. This could be due to several factors such as relatively lower crystallinity, weak contact between the substrate and emitters, and lower conductivity of nanostructures obtained in a low-temperature growth process. The turn-on field obtained from the nanospikes in the present work is found to be lower (i.e., better) than the electrochemically synthesized ZnO nanowire nanoarrays via a template (3.9 V/$\mu$m) (11), ZnO nanowires without (15.5 V/$\mu$m) and with post-hydrogen plasma treatment (9.5 V/$\mu$m), and ZnO films (16.9 V/$\mu$m) (10). The observed turn-on field also appears to be better than not only nanoneedles and nanorods (12), as well as nanotubes (13) synthesized hydrothermally, but also ZnO nanorods (6.5 V/$\mu$m) grown using an anodic aluminum oxide template by atomic layer deposition at 250 °C (65) and nanoneedles (4.1 V/$\mu$m) grown on polyamide using filtered cathodic vacuum arc deposition (66). The better FE performance from nanospikes over other nanostructures mentioned above may be due to better-defined crystalline structure and tip shape (as discussed in detail below). In the case of hydrothermally synthesized nanonunchakus (14) and nanorods (15, 16), all of which appear to exhibit a lower turn-on field than the nanospikes, the synthesis usually employs a more complicated process involving metal nanoparticles and/or metal substrates. Furthermore, a slightly higher synthesis temperature (95−160 °C) and a longer deposition time than that used by electrodeposition are required. Another advantage of electrodeposition over the hydrothermal method is the use of conductive substrates, which could facilitate selective patterned deposition of nanostructures appropriate for FE applications. Moreover, although the turn-on field of the nanospikes electro-

chemically synthesized at 70 °C in the present work is higher than that of the ZnO nanostructures obtained by thermal evaporation methods shown in Table 2, it is still lower than the majority of the ZnO nanostructures, including nanoneedles (27), nanopencils (28), and nanorods (29) (incomplete list), synthesized at higher temperature reported to date. In addition to the lower turn-on field, the current density of nanospikes is at least 4 times higher (>1.3 mA/cm$^2$ at 7.0 V/$\mu$m and 68 $\mu$A/cm$^2$ at 4.8 V/$\mu$m) than other electrochemically synthesized ZnO nanostructures (<250 $\mu$A/cm$^2$ at 20 V/$\mu$m (10) and 15 $\mu$A/cm$^2$ at 4.8 V/$\mu$m (11)) reported recently and is also comparable to that of most ZnO nanostructures obtained by thermal evaporation methods. It is important to note that, despite their better FE performance, none of these CVD and hydrothermally prepared ZnO nanostructures has been deposited on a glass substrate (generally recognized to be more robust and less expensive than silicon). The present electrochemically synthesized ZnO nanospikes on ITO glass, therefore, offer a promising material platform to develop low-cost display applications.

FE from a conventional emitter is based on the model of a cylinder, cone, pyramid, or hemispheroid of height $h$ and radius $r$. The intrinsic field enhancement factor $\beta$ of such an individual emitter is related to the aspect ratio $h/r$. However, in the case of nanostructured emitters, the $h/r$ ratio is found to be less important in assessing the emission behavior (20). In the present work, the $h/r$ ratio for nanospikes is measured to be smaller (8.3) than that of nanopillars (10.9). However, the experimental $\beta$ value for nanospikes is found to be much higher (2364) than that of nanopillars (1170), indicating that other geometrical factors of nanoemitters may play a major role. She et al. have done detailed investigations of the FE properties from ZnO nanostructures of different geometrical shapes and conductivity (70). The surface work function, the resistance of emitters, and the electrical field intensity at the emitter tip are important factors that determine the FE properties (70). Considering that both the nanospikes and nanopillars are well crystalline (as seen in the HRTEM images in Figure 2), the surface work function may be similar. In general, the higher the resistance of the emitter, the poorer is the emission because of the restricted movement of electrons from the back surface of the emitter to the tip. Because we have not measured the resistance of as-synthesized nanospikes and nanopillars, the different behavior of FE is discussed on the basis of the geometrical shapes of the emitters. The low turn-on field and high current density from nanospikes compared to nanopillars have been attributed to two important factors: tip shape and spatial density. The emitter tip can be of various shapes with different tip cone angles ($\theta$) and tip radii ($R_{tip}$) that control the emission properties, i.e., smaller $\theta$ and $R_{tip}$ are more suitable for high FE (20, 71). As shown schematically in Figure 8, the $\theta$ and $R_{tip}$ values of the nanospikes and nanopillars, as measured from Figure 1, are 60° and 20−50 nm and 180° and 100−120 nm, respectively. Both of the $\theta$ and $R_{tip}$ values for the nanospikes are evidently smaller than those of the nanopillars, which is in agreement with the higher FE properties obtained from the

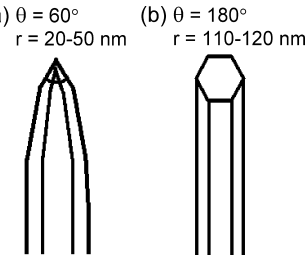


**FIGURE 8. Geometrical shapes of a field emitter for (a) nanospikes and (b) nanopillars.**

nanospikes. Furthermore, electron emission can be greatly increased by creating an appropriate spatial density of sharp tips or protrusions on a flat cathode surface (64, 72−74). Reduction in emission could occur when sharp peaks are densely packed, because of the screening effect that prevents the field from concentrating on the tips of the emitters. Reduction in emission could also occur if the spatial density of the emitters is below a certain limit (64, 73, 74). Given that the separations among the tips of nanospikes are 0.5−1.0 $\mu$m (Figure 1a−c) while those of the nanopillars are less than 200 nm (Figure 1d−f), the screening effect could account for the observed reduced emission performance of nanopillars more than nanospikes. Correspondingly, the field enhancement factor of nanopillars is almost half that of nanospikes. A similar observation has been made with a high density of ZnO nanowires exhibiting lower emission as compared to a medium density (64, 73, 74). Even though nanospikes have a larger amount of surface hydroxide as compared to nanopillars, the smaller tips and higher spatial density of nanospikes play an important role for their superior FE properties. Further improvement of the FE properties may be possible by the removal of surface hydroxide and the fabrication of more ordered growth of nanospikes, and the effort in this direction is currently in progress.

## 4. CONCLUSIONS

In the present work, we demonstrate electrochemical growth of two different types of 1D ZnO nanostructures on ITO glass substrate at 70 °C, including nanospikes in the form of globular bunches and uniformly distributed, well-aligned nanopillars with a hexagonal shape. XRD and HRTEM studies reveal that these 1D ZnO nanostructures have the wurtzite structure with preferential growth in the (0001) plane. Raman scattering measurement indicates the presence of defects and oxygen vacancies, which could also be responsible for the observed PL in the visible region. XPS studies confirm the presence of $Zn(OH)_2$ with a smaller hydroxide percentage in ZnO nanopillars than nanospikes. Furthermore, the low-temperature synthesized nanospikes exhibit superior FE properties on an ITO glass substrate for the first time, with a lower turn-on field than those reported for most other 1D ZnO nanostructured materials obtained by thermal evaporation techniques. The remarkably high FE current density (1.0 mA/cm$^2$ at 6.6 V/$\mu$m) promises these ZnO nanospikes deposited on ITO glass at a low temperature (70 °C) to be good candidates for use in low-cost large-area display applications.

**Acknowledgment.** This work was supported by the Natural Sciences and Engineering Research Council of Canada and the Japan Society for the Promotion of Science (Grants-in-aid for Scientific Research No. 18560661).

## REFERENCES AND NOTES


(1) Coleman, V. A.; Jagadish, C. *Basic properties and applications of ZnO in Zinc Oxide Bulk, Thin films and Nanostructures*; Jagadish, C., Pearton, S. J., Eds.; Elsevier Publications: New York, 2006; Chapter 1.
(2) Gao, P. X.; Lao, C. S.; Ding, Y.; Wang, Z. L. *Adv. Funct. Mater.* **2006**, *16*, 53, and references cited therein. .
(3) Vayssieres, L. *Adv. Mater.* **2003**, *15*, 464.
(4) Tian, Z. R.; Voigt, J. A.; Liu, J.; Mckenzie, B.; Mcdermott, M. J.; Rodriguez, M. A.; Konishi, H.; Xu, H. *Nat. Mater.* **2003**, *2*, 821.
(5) Peulon, S.; Lincot, D. *Adv. Mater.* **1996**, *8*, 166.
(6) Lopez, C. M.; Choi, K. S. *Chem. Commun.* **2005**, 3328.
(7) Levy-Clement, C.; Tena-Zaera, R.; Ryan, M. A.; Katty, A.; Hodes, G. *Adv. Mater.* **2005**, *17*, 1512.
(8) Law, M.; Greene, L. E.; Johnson, J. C.; Saykally, R.; Yang, P. *Nat. Mater.* **2005**, *4*, 455.
(9) Cheng, A.-J.; Wang, D.; Seo, H. W.; Liu, C.; Park, M.; Tzeng, Y. *Diamond Relat. Mater.* **2006**, *15*, 426.
(10) Cao, B.; Teng, X.; Heo, S. H.; Li, Y.; Cho, S. O.; Li, G.; Cai, W. *J. Phys. Chem. C* **2007**, *111*, 2470.
(11) Xu, C. X.; Sun, X. W.; Fang, S. N.; Yang, X. H.; Yu, M. B.; Zhu, G. P.; Cui, Y. P. *Appl. Phys. Lett.* **2006**, *88*, 161921.
(12) Liu, J.; Huang, X.; Li, Y.; Ji, X.; Li, Z.; He, X.; Sun, F. *J. Phys. Chem. C* **2007**, *111*, 4990.
(13) Wei, A.; Sun, X. W.; Xu, C. X.; Dong, Z. L.; Yu, M. B.; Huang, W. *Appl. Phys. Lett.* **2006**, *88*, 213102.
(14) Hu, H.; Yu, K.; Zhu, J.; Zhu, Z. *Appl. Surf. Sci.* **2006**, *252*, 8410.
(15) Ye, C.; Bando, Y.; Fang, X.; Shen, G.; Golberg, D. *J. Phys. Chem. C* **2007**, *111*, 12673.
(16) Marathe, S. K.; Koinkar, P. M.; Ashtaputre, S. S.; More, M. A.; Gosavi, S. W.; Joag, D. S.; Kulkarni, S. K. *Nanotechnology* **2006**, *17*, 1932.
(17) Li, C.; Fang, G.; Liu, N.; Li, J.; Liao, L.; Su, F.; Li, G.; Wu, X.; Zhao, X. *J. Phys. Chem. C* **2007**, *111*, 12566.
(18) Li, C.; Yang, Y.; Sun, X. W.; Lei, W.; Zhang, X. B.; Wang, B. P.; Wang, J. X.; Tay, B. K.; Ye, J. D.; Lo, G. Q.; Kwong, D. L. *Nanotechnology* **2007**, *18*, 135604.
(19) Huo, K.; Hu, Y.; Fu, J.; Wang, X.; Chu, P. K.; Hu, Z.; Chen, Y. *J. Phys. Chem. C* **2007**, *111*, 5876.
(20) Yang, Y. H.; Wang, B.; Xu, N. S.; Yang, G. W. *Appl. Phys. Lett.* **2006**, *89*, 043108.
(21) Jo, S. H.; Banerjee, D.; Ren, Z. F. *Appl. Phys. Lett.* **2004**, *85*, 1407.
(22) Wang, W.; Zeng, B.; Yang, J.; Poudel, B.; Huang, J.; Naughton, M. J.; Ren, Z. *Adv. Mater.* **2006**, *18*, 3275.
(23) Xu, C. X.; Sun, X. W. *Appl. Phys. Lett.* **2003**, *83*, 3806.
(24) Yu, K.; Zhang, Y.; Xu, R.; Ouyang, S.; Li, D.; Luo, L.; Zhu, Z.; Ma, J.; Xie, S.; Han, S.; Geng, H. *Mater. Lett.* **2005**, *59*, 1866.
(25) Xu, F.; Yu, K.; Li, Q.; Zhu, Z.; Yao, T. *J. Phys. Chem. C* **2007**, *111*, 4099.
(26) Park, C. J.; Choi, D. K.; Yoo, J.; Yi, G. C.; Lee, C. J. *Appl. Phys. Lett.* **2007**, *90*, 83107.
(27) Tseng, Y.-K.; Huang, C.-J.; Cheng, H.-M.; Lin, I.-N.; Liu, K.-S.; Chen, I.-C. *Adv. Funct. Mater.* **2003**, *13*, 811.
(28) Shen, G.; Bando, Y.; Liu, B.; Golberg, D.; Lee, C. J. *Adv. Funct. Mater.* **2006**, *16*, 410.
(29) Li, L. M.; Du, Z. F.; Li, C. C.; Zhang, J.; Wang, T. H. *Nanotechnology* **2007**, *18*, 355606.
(30) Pradhan, D.; Leung, K. T. *J. Phys. Chem. C* **2008**, *112*, 1357.
(31) Cao, B.; Li, Y.; Duan, G.; Cai, W. *Cryst. Growth Des.* **2006**, *6*, 1091.
(32) Chen, Q.-P.; Xue, M.-Z.; Sheng, Q.-R.; Liu, Y.-G.; Ma, Z.-F. *Electrochem. Sol. State Lett.* **2006**, *9*, C58.
(33) Pauporte, T.; Lincot, D.; Viana, B.; Pelle, F. *Appl. Phys. Lett.* **2006**, *89*, 233112.
(34) JCPDS file reference number 01-076-0704, PDF-2 Database, International Center for Diffraction Data (ICDD), 2004.
(35) Wu, J.-J.; Liu, S.-C. *Adv. Mater.* **2002**, *14*, 215.
(36) Pradhan, A. K.; Williams, T. M.; Zhang, K.; Hunter, D.; Dadson, J. B.; Lord, K.; Roy, U. N.; Cui, Y.; Burger, A. *J. Nanosci. Nanotechnol.* **2006**, *6*, 1985.
(37) Deroubaix, G.; Marcus, P. *Surf. Interface Anal.* **1992**, *18*, 39.
(38) Au, C. T.; Roberts, M. W.; Zhu, A. R. *Surf. Sci.* **1982**, *115*, L117.
(39) Bär, M.; Reichardt, J.; Sieber, I.; Grimm, A.; Kötschau, I.; Lauermann, I.; Sokoll, S.; Lux-Steiner, M. C.; Fischer, C. H.; Niesen, T. P. *J. Appl. Phys.* **2006**, *100*, 23710.
(40) Liu, B.; Zeng, H. C. *J. Am. Chem. Soc.* **2004**, *126*, 16744.
(41) Moulder, J. F.; Stickle, W. F.; Sobol, P. E.; Bomben, K. D. In *Handbook of X-ray Photoelectron Spectroscopy*; Chastain, J., Ed.; Perkin-Elmer Corp., New York, 1992.
(42) Damen, T. C.; Porto, S. P. S.; Tell, B. *Phys. Rev.* **1966**, *142*, 570.
(43) Chen, Z. Q.; Kawasuso, A.; Xu, Y.; Naramoto, H.; Yuan, X. L.; Sekiguchi, T.; Suzuki, R.; Ohdaira, T. *J. Appl. Phys.* **2005**, *97*, 13528.
(44) Mcguire, K.; Pan, Z. W.; Wang, Z. L.; Milkie, D.; Menendez, J.; Rao, A. M. *J. Nanosci. Nanotechnol.* **2002**, *2*, 499.
(45) Xu, C.; Kim, M.; Chun, J.; Kim, D. *Appl. Phys. Lett.* **2005**, *86*, 133107.
(46) Rajalakshmi, M.; Arora, A. K.; Bendre, B. S.; Mahamuni, S. *J. Appl. Phys.* **2000**, *87*, 2445.
(47) Mari, B.; Manjon, F. J.; Mollar, M.; Cembrero, J.; Gomez, R. *Appl. Surf. Sci.* **2006**, *252*, 2826.
(48) Xu, C.; Rho, K.; Chun, J.; Kim, D.-E. *Appl. Phys. Lett.* **2005**, *87*, 253104.
(49) Yumato, H.; Kaneko, T.; Hasiguti, R. R.; Watanabe, T. *J. Cryst. Growth* **1987**, *84*, 185.
(50) Yu, J.; Xing, H.; Zhao, Q.; Mao, H.; Shen, Y.; Wang, J.; Lai, Z.; Zhu, Z. *Solid State Commun.* **2006**, *138*, 502.
(51) Decremps, F.; Pellicer-Porres, J.; Saitta, A. M.; Chervin, J. C.; Polian, A. *Phys. Rev. B* **2002**, *65*, 092101.
(52) Calleja, J. M.; Cardona, M. *Phys. Rev. B* **1977**, *16*, 3753.
(53) Alim, K. A.; Fonoberov, V. A.; Shamsa, M.; Balandin, A. A. *J. Appl. Phys.* **2005**, *97*, 124313.
(54) Chen, Y. W.; Liu, Y. C.; Lu, S. X.; Xu, C. S.; Shao, C. L.; Wang, C.; Zhang, J. Y.; Lu, Y. M.; Shen, D. Z.; Fan, X. W. *J. Chem. Phys.* **2005**, *123*, 134701.
(55) Lin, B.; Fu, Z.; Jia, Y. *Appl. Phys. Lett.* **2001**, *79*, 943.
(56) Djurišić, A. B.; Choy, W. C. H.; Roy, V. A. L.; Leung, Y. H.; Kwong, C. Y.; Cheah, K. W.; Gundu Rao, T. K.; Chan, Y. K.; Lui, H. F.; Surya, C. *Adv. Funct. Mater.* **2004**, *14*, 856, and references cited therein.
(57) Umar, A.; Kim, S. H.; Suh, E. K.; Hahn, Y. B. *Chem. Phys. Lett.* **2007**, *440*, 110.
(58) Studenikin, S. A.; Golego, N.; Cocivera, M. *J. Appl. Phys.* **1998**, *84*, 2287.
(59) Djurišić, A. B.; Leung, Y. H.; Tam, K. H.; Ding, L.; Ge, W. K.; Chen, H. Y.; Gwo, S. *Appl. Phys. Lett.* **2006**, *88*, 103107.
(60) Meng, X. Q.; Shen, D. Z.; Zhang, J. Y.; Zhao, D. X.; Lu, Y. M.; Dong, L.; Zhang, Z. Z.; Liu, Y. C.; Fan, X. W. *Solid State Commun.* **2005**, *135*, 179.
(61) Mahamuni, S.; Borgohain, K.; Bendre, B. S.; Leppert, V. J.; Risbud, S. H. *J. Appl. Phys.* **1999**, *85*, 2861.
(62) Hu, J. Q.; Ma, X. L.; Xie, Z. Y.; Wong, N. B.; Lee, C. S.; Lee, S. T. *Chem. Phys. Lett.* **2001**, *344*, 97.
(63) Vanheusden, K.; Warren, W. L.; Seager, C. H.; Tallant, D. R.; Voigt, J. A.; Gnade, B. E. *J. Appl. Phys.* **1996**, *79*, 7983.
(64) Liu, J.; She, J.; Deng, S.; Chen, J.; Xu, N. S. *J. Phys. Chem. C* **2008**, *112*, 11685.
(65) Yang, C.-J.; Wang, S.-M.; Liang, S.-W.; Chang, Y.-H.; Chen, C.; Shieh, J.-M. *Appl. Phys. Lett.* **2007**, *90*, 033104.
(66) Yang, H. Y.; Lau, S. P.; Yu, S. F.; Huang, L.; Tanemura, M.; Tanaka, J.; Okita, T.; Hng, H. H. *Nanotechnology* **2005**, *16*, 1300.
(67) Banerjee, D.; Jo, S. H.; Ren, Z. F. *Adv. Mater.* **2004**, *16*, 2028.
(68) Wang, R. C.; Liu, C. P.; Huang, J. L.; Chen, S.-J.; Tseng, Y.-K.; Kung, S.-C. *Appl. Phys. Lett.* **2005**, *87*, 013110.
(69) Liao, L.; Li, J. C.; Liu, D. H.; Liu, C.; Wang, D. F.; Song, W. Z.; Fu, Q. *Appl. Phys. Lett.* **2005**, *86*, 083106.
(70) She, J.; Xiao, Z.; Yang, Y.; Deng, S.; Chen, J.; Yang, G.; Xu, N. *ACS Nano* **2008**, *2*, 2015.
(71) Utsumi, T. *IEEE Trans. Electron Dev.* **1991**, *38*, 2276.
(72) Jo, S. H.; Lao, J. Y.; Ren, Z. F.; Farrer, R. A.; Baldacchini, T.; Fourkas, J. T. *Appl. Phys. Lett.* **2003**, *83*, 4821.
(73) Wang, X.; Zhou, J.; Lao, C.; Song, J.; Xu, N.; Wang, Z. L. *Adv. Mater.* **2007**, *19*, 1627.
(74) Li, C.; Di, Y.; Lei, W.; Yin, Q.; Zhang, X.; Zhao, Z. *J. Phys. Chem. C* **2008**, *112*, 13447.


AM800220V